Nexus of Future Materials

https://nfmjournal.com/

Exploration of the Crystal Structure and Impedance Spectroscopy Characteristics in $Ba_{0.54}Na_{0.46}Nb_{1.29}W_{0.37}O_5$ Crystalline Phase

H. Es-soufi[1,2,3] *, A. Lahmar[4], R. Rajesh[5], H. Bih[6], L. Bih[3]

[1] *National Higher School of Chemistry (NHSC), Ibn Tofaïl University, BP. 133-14000, Kenitra, Morocco*
[2] *Laboratory of Organic, Inorganic Chemistry, Electrochemistry and Environment, Faculty of Sciences, Ibn Tofaïl University, PO Box 133-14000, Kenitra, Morocco*
[3] *Laboratory of Sciences and Professions of the Engineer, Materials and Processes Department ENSAM-Meknes Marjane II, Moulay Ismail University, El Mansour, Meknes P.O. Box 15290, Morocco*
[4] *Condensed Matter Physics Laboratory, University of Picardie Jules Verne, Amiens, France*
[5] *Department of Physics, Velammal College of Engineering & Technology, Madurai 625009, India*
[6] *Process Engineering, Computer Science and Mathematics Laboratory (LIPIM), National School of Applied Engineering-Khouribga, Sultan Moulay Slimane University, Beni Mellal 23000, Morocco*

Keywords:

Solid-state method
Crystal structure analysis
X-ray diffraction
Rietveld method
Impedance spectroscopy
Non-Debye conductivity relaxation

Abstract

In this study, a solid-state approach was utilized to synthesize $Ba_{0.54}Na_{0.46}Nb_{1.29}W_{0.37}O_5$ ceramic material. The crystal structure of the synthesized material was examined through X-ray diffraction, with further refinement carried out using the Rietveld method. The analysis revealed that the material exhibited a crystal structure resembling tungsten tetragonal bronze. The determined cell parameters were found to be $a = b = 12.37813 \pm 0.02$ Å and $c = 3.93552 \pm 0.02$ Å, with a space group of P4bm. Electrical investigations were conducted via impedance spectroscopy across a frequency range from 1 Hz to 1 MHz, and a temperature range from ambient to 550 °C. The analysis of the impedance data indicated a distinct non-Debye conductivity relaxation behavior within this crystalline phase. Interestingly, the electrical response was attributed to dual contributions from both the grains and their boundaries, as well as the electrodes.

1. Introduction

Tetragonal tungsten bronze (TTB) represents a distinctive ceramic material, characterized by an exclusive crystal arrangement comprising interconnected tungsten oxide octahedra, forming a structural lattice [1-2].

This unique TTB crystal formation gives rise to a range of captivating attributes, encompassing a remarkable dielectric constant, piezoelectric behavior, and ferroelectric properties [3]. Notably, TTB's elevated dielectric constant positions it as an optimal contender for capacitors, integral components within electronic apparatus, serving to accumulate electrical energy. The piezoelectric trait inherent in TTB enables it to generate an electric charge when subjected to mechanical stress, showcasing its utility in pressure, acceleration, and vibration sensing technologies. Meanwhile, TTB's ferroelectric quality grants it a lasting electric dipole moment, facilitating applications such as non-volatile memory and energy accumulation. Collectively, TTB's distinct characteristics establish it as a versatile substance for diverse applications spanning electronics, sensor technologies, and energy retention [4]. Specifically categorized as a variant of tungsten bronze, TTB is located within the family of materials featuring tungsten oxide octahedra organized in a specific crystal configuration [5]. Within this class, TTB is classified as an ABO_3 perovskite-like compound, where "A" commonly signifies an alkali or alkaline earth metal, and "B" represents a transition metal [6]. The unique TTB crystal structure encompasses corner-connected tungsten oxide octahedra that

* Corresponding author:
E-mail address: hichamessoufi@gmail.com

Received 19 January 2024; Accepted 11 March 2024;
Published 13 March 2024
https://nfmjournal.com/articles/6

compose a three-dimensional (3D) framework, ultimately giving rise to its distinct features, such as the high dielectric constant, piezoelectricity, and ferroelectric nature [7]. TTB materials, also recognized as niobium-tungsten-oxide (Nb-W-O) materials, exhibit intricate impedance characteristics attributed to their distinct electronic and structural attributes [8]. These impedance characteristics find their foundation in the electronic composition, characterized by both metallic and insulating states. Metallic states emerge from the partially occupied tantalum and tungsten d-orbitals, while the insulating states find their origin in the oxygen p-orbitals. As a result of this electronic structure, heightened conductivity occurs in the metallic states, in contrast to the low conductivity within the insulating states [9]. Beyond the electronic realm, TTB materials' crystalline arrangement plays a vital role in shaping their impedance traits. The intricate 3D crystal framework encompasses interlinked tunnels and pathways that act as conduits for ion diffusion. These conduits expedite ion movement and consequently contribute to elevated ionic conductivity at lower temperatures [10]. Collectively, TTB materials' impedance characteristics emerge as auspicious candidates for a multitude of applications, spanning energy storage, catalysis, and electrochromic devices. One illustrative instance involves their application as electrode materials within lithium-ion batteries, revealing impressive cycling stability and high-rate capabilities [11].

This investigation synthesizes the $Ba_{0.54}Na_{0.46}Nb_{1.29}W_{0.37}O_5$ compound by utilizing a solid-state approach. Subsequently, the Rietveld refinement technique, facilitated by the Full Prof software, is employed to decipher the crystalline parameters and structure from the X-ray diffraction (XRD) data. Furthermore, an evaluation of the electrical attributes of this crystalline phase is undertaken, employing impedance spectroscopy.

In conclusion, our investigation synthesizes and characterizes the $Ba_{0.54}Na_{0.46}Nb_{1.29}W_{0.37}O_5$ compound using a solid-state approach, combined with a comprehensive analysis of its crystalline parameters and structure through the Rietveld refinement technique and XRD data, thus providing valuable insights into the unique properties of TTB materials.

The results obtained from this study make a significant contribution to the existing literature on TTB materials, particularly shedding light on the electronic and structural attributes that govern their impedance characteristics. By elucidating the intricate interplay between metallic and insulating states within TTB materials, our understanding of their conductivity profiles had been enhanced, paving the way for applications in diverse fields. Furthermore, our investigation extends beyond the electronic realm to explore the role of the crystalline arrangement in shaping impedance traits. The 3D crystal framework of TTB materials, characterized by interlinked tunnels and pathways facilitating ion diffusion, presents promising prospects for applications such as energy storage, catalysis, and electrochromic devices.

The successful synthesis of the $Ba_{0.54}Na_{0.46}Nb_{1.29}W_{0.37}O_5$ compound and the detailed analysis of its electrical attributes through impedance spectroscopy not only enhance our comprehension of TTB materials, but also provide a foundation for future research endeavors. The findings emerging from this study can guide the development of improved electrode materials for lithium-ion batteries, offering enhanced cycling stability and high-rate capabilities.

In summary, this investigation not only contributes to the fundamental understanding of TTB materials but also opens avenues for practical applications, aligning with the ongoing efforts to advance materials science and technology. As we continue to explore and harness the unique properties of TTB compounds, the implications of this research extend to various fields, including electronics, sensor technologies, energy storage, and beyond.

2. Experimental part

2.1. Sample preparation

Starting from the raw materials $BaCO_3$, $NaCO_3$, WO_3, and Nb_2O_5, sourced from Merck at a purity of 99.95%, the crystalline phase $Ba_{0.54}Na_{0.46}Nb_{1.29}W_{0.37}O_5$ was synthesized. Initially, these raw components were ground for 1 h using an agate mortar. Subsequently, the resulting mixture was placed in an alumina crucible and subjected to a 24-h heating process at 600 °C. After this step, the mixture was once again, ground for approximately 1 h, this time with ethanol, in preparation for the calcination stage. The calcination process was conducted in an alumina crucible, maintaining a final heating temperature of 1300 °C for 24 h. The grinding and calcination procedures were repeated twice to complete the chemical processing of the compounds. The purity and formation of the resulting chemical compound were evaluated using XRD analysis.

The phase formation of the prepared sample was investigated using an X-ray diffractometer (Bruker D8 Advance) at room temperature. CuKα radiation (wavelength: 0.1540598 nm) was employed, and the scanning was performed at a rate of 4°/min within a 2θ range of $10 - 100, ℃$ utilizing a step size of 0.01. The Rietveld pattern analysis method was augmented through the utilization of the Full Prof software [12].

For the purpose of dielectric measurement, the disk-shaped samples underwent a polishing procedure. To establish optimal electrical contact, silver paste was subsequently applied to both sides of each specimen. The capacitance (C_p) and dissipation factor $(\tan\delta)$ were measured across a frequency range of 20 Hz to 1 MHz using an impedance analyzer. The electrode pellets were supplied with a 0.5 V source. The measurements were performed utilizing a Linkam TS 93 hot stage, known for its temperature stability of 0.1 K. The temperature range for the measurements spanned 25–550 °C. To create capacitor-shaped samples, platinum electrodes were affixed to two opposing cylindrical faces of the ceramic material. As a result, equations 1 and 2 were employed to calculate the real part of the dielectric constant (ε') and the dielectric loss $(\tan\delta)$, respectively [13].

$$\varepsilon' = \frac{C_p t}{\varepsilon_0 A} \quad (1)$$

$$\tan\delta = \frac{\varepsilon''}{\varepsilon'} \quad (2)$$

where "t" symbolizes the thickness of the sample in the shape of a disk, "A" corresponds to the cross-sectional electrode area, "ω" pertains to the angular frequency, "ε_0" stands for the permittivity of empty space, and "ε" (calculated as "ε" multiplied by the tangent of $\tan\delta$) represents the component of the complex dielectric constant that is imaginary.

The values of dielectric parameters, namely, the real component of the dielectric constant $(\varepsilon'(\omega))$ and the imaginary component of the dielectric constant $(\varepsilon'^{(\omega)})$, play a crucial role in calculating the complex formalism parameters $Z'(\omega)$ and $Z''(\omega)$ using equation (3) [13]:

$$j\omega C_0\big(Z'(\omega) + Z''(\omega)\big) = \varepsilon'(\omega) + j\varepsilon''(\omega)$$

Where, "C_0" denotes the capacitance of a vacuum. The data underwent analysis using the Zview software and was subsequently visualized through the utilization of the intricate plane framework portraying $Z'(\omega)$ against $Z''(\omega)$. The Zview software, specifically engineered for the interpretation of equivalent electric circuits and the fitting of emittance spectra data [14], was employed for this purpose. The impedance characteristics of ceramic materials find representation in the form of

$$Z^*(\omega) = Z_g(\omega) + Z_{gb}(\omega) + Z_{elect}(\omega)$$

Where, $Z_g(\omega)$, $Z_{gb}(\omega)$, and $Z_{elect}(\omega)$ respectively indicate the impedance of the grains, grain boundaries, and electrodes.

3. Results and discussion

3.1 Analysis of the XRD and Rietveld refinement

Fig. 1 illustrates the Rietveld refinement patterns for the $Ba_{0.54}Na_{0.46}Nb_{1.29}W_{0.37}O_5$ ceramic, which underwent sintering at 1300 °C for a duration of 12 h. The figure clearly reveals a remarkable agreement between the computed and observed diffractograms, underscoring the robustness of the results. The pattern unambiguously substantiates the existence of a solitary phase characterized by a TTB configuration, devoid of any impurity phases. The parameters obtained through the Rietveld refinement method, operating within the P4bm space group, demonstrate congruence with earlier findings. Specifically, the lattice constants a and b measure 12.37813 ± 0.02 Å, while c stands at 3.93552 ± 0.02 Å. It is noteworthy that these parameters align closely with the outcomes attained in our previous study [16] using both the Full Prof and GSASII software, thus affirming their consistency.

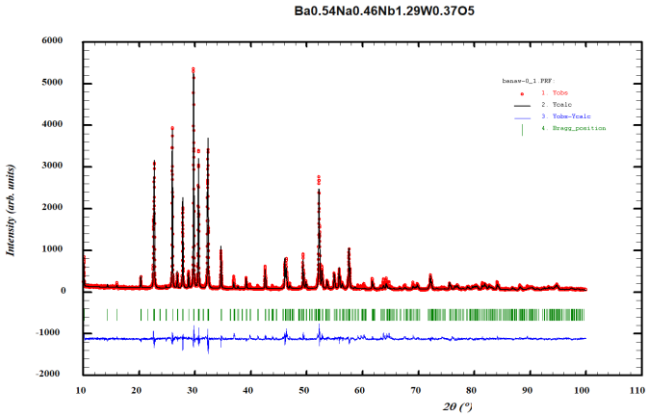

Fig. 1. Crystal structure analysis of $Ba_{0.54}Na_{0.46}Nb_{1.29}W_{0.37}O_5$ using Rietveld refinement.

3.2. Complex impedance spectroscopy

Fig. 2(a) illustrates plots of Z′ against frequency across various temperatures, displaying three distinct characteristics: i) A decline in the Z′ value with increasing frequency, implying reduced AC resistivity in the $Ba_{0.54}Na_{0.46}Nb_{1.29}W_{0.37}O_5$ ceramic. i) A decrease in the Z′ value as the temperature rises, signifying enhanced conduction. ii) Consistent Z′ values in the higher frequency range, suggesting possible space charge release [17-19].

Moving to Fig. 2(b), the impedance loss spectrumZ″ vs f is depicted at different temperatures, with analysis of this figure revealing two key insights: i) The peak values of Z″ decrease with temperature elevation, indicating higher loss $(\tan\delta)$ in the sample's resistive property (bulk resistance). This relationship is due to tan δ being directly proportional to

$\left(\frac{1}{Z'}\right)$ [20]. *ii*) The presence of asymmetrically broadening peaks shifting to higher frequency regions with rising temperature. This shift points to a temperature-dependent relaxation mechanism within the sample [19-21]. This mechanism stems from immobile electrons/species at lower temperatures and vacancies/defects at higher temperatures [19].

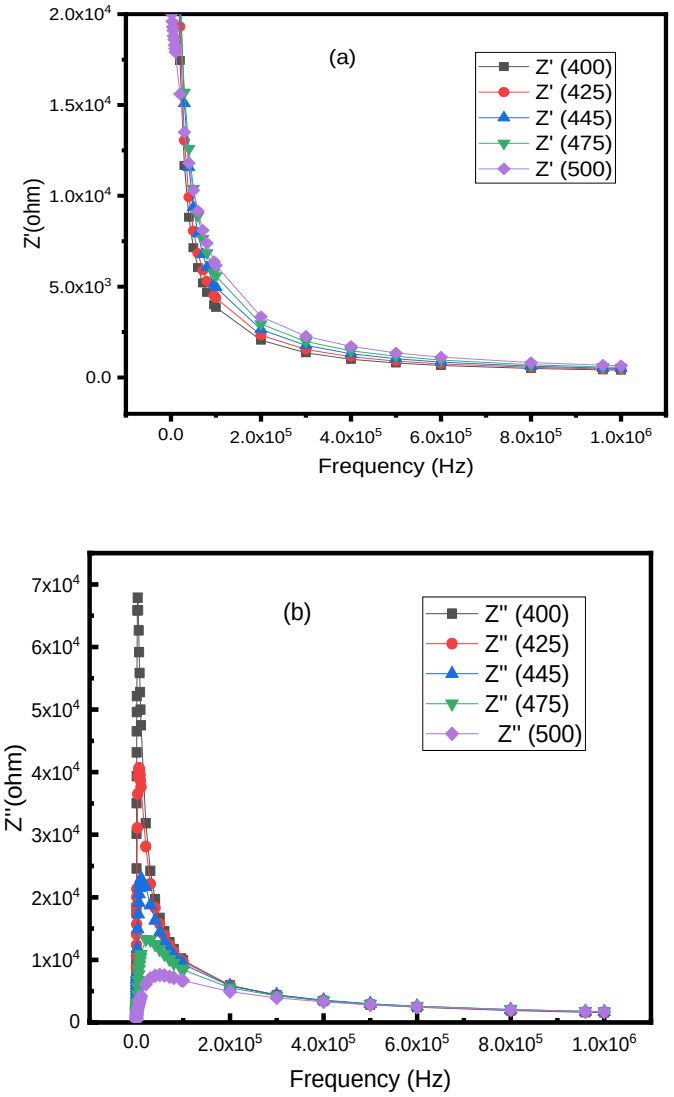

Fig. 2. Observing variations in impedance components (Z' and $-Z''$) across different temperatures and frequencies.

Furthermore, the utilization of complex impedance analysis led to the application of the Cole–Cole or Nyquist plot for investigating the previously mentioned mechanism, as depicted in Fig. 3. At varying temperatures, a distinctive single semi-circular arc was discerned. This particular pattern has been documented in numerous studies, where the impedance response is primarily shaped by parallel R_c components. Notably, one of the resistances exhibits a remarkably higher value, attributed to the presence of grains or grain boundaries, resulting in a substantial discrepancy in resistance [17, 22-24].

In contrast, when the resistance values are akin due to grains or grain boundaries, the visual representation reveals two separate semicircular arcs of equal magnitude [23]. If a semicircle is off-center with its midpoint positioned below the x-axis, this indicates a form of relaxation that is not in line with Debye-type behavior. As a result, it can be deduced that the electrical traits emanate from the influences of grains and grain boundaries. This outcome effectively validates the existence of grain boundaries in the $Ba_{0.54}Na_{0.46}Nb_{1.29}W_{0.37}O_5$ ceramic material.

To distinguish among the dielectric attributes of the grains, grain boundaries, and electrodes within the ceramic material, a plausible approach involves modeling the material as a sequence of three parallel R_c-components connected in series, as portrayed in Fig. 4. The first component of this model signifies the dielectric characteristics of the grains, the second component represents the dielectric properties of the grain boundaries, and the final component embodies the dielectric attributes of the electrodes, referred to as R_{elect} [25]. However, the approximation of R_{gb} surpasses that of R_g significantly, indicating that the overall resistance of the $Ba_{0.54}Na_{0.46}Nb_{1.29}W_{0.37}O_5$ ceramic is predominantly governed by R_{gb} due to its blocking effect. This phenomenon is commonly denoted as "the blocking effect of the grain boundary" [26]. Similar observations have been documented in previously published literature [27].

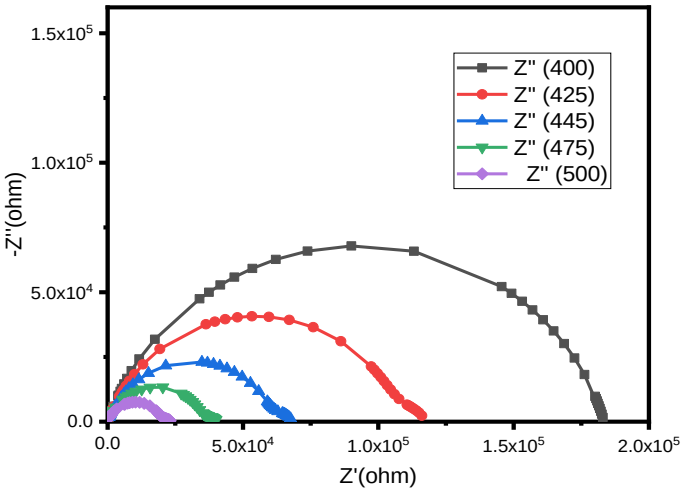

Fig. 3. Temperature-dependent Cole–Cole analysis of the $Ba_{0.54}Na_{0.46}Nb_{1.29}W_{0.37}O_5$ ceramic: impedance spectroscopy insights.

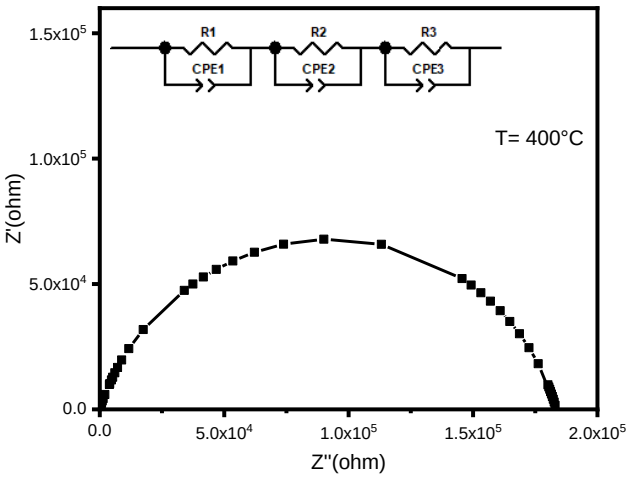

Fig. 4. Curve fitting of the Cole–Cole diagram and distinction among three circuits.

4. Conclusion

In this study, a $Ba_{0.54}Na_{0.46}Nb_{1.29}W_{0.37}O_5$ ceramic, meticulously prepared using the solid-state technique, became the focal point of investigation. The core objectives encompassed a comprehensive exploration of both its structural attributes and electrical properties. The culmination of these endeavors yielded a series of discerning conclusions, encapsulated as follows:

i) The intricate utilization of the Rietveld refinement method bore fruit, as the derived parameters shed light on the crystalline essence of the $Ba_{0.54}Na_{0.46}Nb_{1.29}W_{0.37}O_5$ compound. It was unequivocally revealed that this compound elegantly adopted a TTB structural motif, intimately associated with the P4bm space group. This profound revelation constitutes a significant milestone in our understanding of the material's inherent architecture. ii) An equally insightful revelation emerged through the deployment of the Cole–Cole diagram, which enabled a nuanced differentiation among the constituent elements within the ceramic matrix. This distinction was not limited to mere physical boundaries, but rather extended to include the grains, grain boundaries, and even the electrodes present within the intricate fabric of the material. This nuanced discrimination significantly contributes to our grasp of the material's internal dynamics, thus underpinning its electrical behavior.

This comprehensive investigation into the $Ba_{0.54}Na_{0.46}Nb_{1.29}W_{0.37}O_5$ ceramic, accomplished through a judicious combination of solid-state preparation, structural analysis, and electrical property exploration, has yielded invaluable insights. The revelations surrounding its crystalline structure and the intricate interplay of its components through advanced diagrammatic analyses are poised to reverberate throughout the realm of ceramic material science, thus inspiring further exploration and innovation.

In conclusion, this comprehensive investigation into the $Ba_{0.54}Na_{0.46}Nb_{1.29}W_{0.37}O_5$ ceramic has not only expanded our understanding of its fundamental properties but also paved the way for future research and applications across diverse scientific and engineering disciplines. The implications of this study resonate beyond the confines of the laboratory, offering potential benefits in a wide range of technological and scientific endeavors.

References

[1] M. Josse, O. Bidault, F. Roulland, E. Castel, A. Simon, D. Michau, R. Von der Mühll, O. Nguyen, M. Maglione, The $Ba_2LnFeNb_4O_{15}$ “tetragonal tungsten bronze”: Towards RT composite multiferroics, Solid State Sciences, 11(2009) 1118-1123.

[2] I. Nylund, C.R. Zeiger, D. Peng, P.E. Vullum, J. Walker, M. Einarsrud, T. Grande, Centrosymmetric Tetragonal Tungsten Bronzes $A_4Bi_2Nb_{10}O_{30}$ (A = Na, K, Rb) with a Bi 6s Lone Pair, Chemistry of Materials, 35(1) (2022) 17–26.

[3] K. Lin, L. You, Q. Li, J. Chen, J. Deng, . Xing, Thermal expansion anomaly in TTB ferroelectrics: The interplay between framework structure and electric polarization, Inorganic Chemistry 55(16) (2016) 8130–8139.

[4] J. Xing, F. Luo, Y. Qin, Y Luo, Z. Gao, F. Shang, G. Chen, $NaSr_2Nb_5O_{15}$: Yb^{3+}, Ho^{3+}, Tm^{3+} transparent glass ceramics: Up-conversion optical thermometry and energy storage property, Journal of the American Ceramic Society, 106(2) (2023) 1074–1088.

[5] M. Belarbi, Y. Tamraoui, B. Manoun, A. Cantaluppi, Y. Gagou, K. Taibi, M. El Marssi, A. Lahmar, Structural, dielectric and energy storage properties of neodymium niobate with tetragonal tungsten bronze structure, Physica B: Condensed Matter, 618 (2021) 413185.

[6] A. Simon, J. Ravez, Solid-state chemistry and non-linear properties of tetragonal tungsten bronzes materials, Comptes Rendus Chimie, 9(10) (2006) 1268–1276.

[7] X. Zhu, M. Fu, M.C. Stennett, P.M. Vilarinho, I. Levin, C.A. Randall, J. Gardner, F.D. Morrison, I.M. Reaney, A crystal-chemical framework for relaxor versus normal ferroelectric behavior in tetragonal tungsten bronzes, Chemistry of Materials, 27(9) (2015) 3250–3261.

[8] D. Delgado, P. Concepción, A. Trunschke, J.M.L Nieto, Tungsten–niobium oxide bronzes: A bulk and surface structural study, Dalton Transactions 49(38) (2020) 13282–13293.

[9] F. Rubio-Marcos, J. J. Romero, M.G. Navarro-Rojero, J.F. Fernandez, Effect of ZnO on the structure, microstructure and electrical properties of KNN-modified piezoceramics, Journal of the European Ceramic Society, 29 (14) (2009) 3045–3052.

[10] M. Leblanc, V. Maisonneuve, A. Tressaud, Crystal chemistry and selected physical properties of inorganic fluorides and oxide-fluorides, Chemical Reviews, 115(2) (2015) 1191–1254.

[11] X. Xiong, L. Yang, G. Liang, Z. Liu, Z. Yang, R. Zhang, C. Wang, R. Che, Cation-vacancy ordered superstructure enhanced cycling stability in tungsten bronze anode, Advanced Energy Materials, 12(36) (2022) 2201967.

[12] The Full Prof Team (n.d.). Crystallographic tools for Rietveld, http://www.ill.eu/sites/fullprof/php/programs.html

[13] B.C. Das, A.K.M.A. Hossain, Rietveld refined structure, ferroelectric, magnetic and magnetoelectric response of Gd-substituted Ni-Cu-Zn ferrite and Ca, Zr co-doped $BaTiO_3$ multiferroic composites, Journal of Alloys and Compounds, 867 (2021)159068.

[14] AMETEK Scientific Instruments. (n.d.). Z View Software. Available at: https://www.ameteksi.com/products/software/zview-software-en

[15] B.H. Toby, R.B.V. Dreele, What's new in GSAS-II, Powder Diffraction, 29 (2014) S2–S6.

[16] H. Es-soufi, H. Bih, L. Bih, R. Rajesh, A.R.F. Lima, M.I. Sayyed, R. Mezher, R. Refinement, Structural Characterization, and Methylene Blue Adsorption of the New Compound $Ba_{0.54}Na_{0.46}Nb_{1.29}W_{0.37}O_5$,Crystals, 12(12) (2022) 1695.

[17] X. Li, T. Shi, B. Li, X. Chen, C. Zhang, Z. Guo, Q. Zhang, Subtractive manufacturing of stable hierarchical micro-nano structures on AA5052 sheet with enhanced water repellence and durable corrosion resistance, Materials & Design, 183 (2019) 108152.

[18] J. Płcharski, W. Weiczorek, PEO based composite solid electrolyte containing nasicon, Solid State Ions, 28–30 (1988) 979-982.

[19] P. Ganguly, A.K. Jha, K.L. Deori, Complex impedance studies of tungsten–bronze structured $Ba_5SmTi_3Nb_7O_{30}$ ferroelectric ceramics, Solid State Communications, 146 (2008) 472-477.

[20] M. Ram, Synthesis and electrical properties of $(LiCo_{3/5}Fe_{1/5}Mn_{1/5})$ VO_4 ceramics, Solid State Sciences, 12 (2010) 350–354.

[21] A.K. Jonscher, The 'universal' dielectric response, Nature, 267 (1977) 673–679.

[22] D.C. Sinclair, A.R. West, Impedance and modulus spectroscopy of semiconducting $BaTiO_3$ showing positive temperature coefficient of resistance, Journal of Applied Physics, 66 (1989) 3850.

[23] D.K. Pradhan, R.N.P. Choudhary, C. Rinaldi, R.S. Katiyar, Effect of Mn substitution on electrical and magnetic properties of $Bi_{0.9}La_{0.1}FeO_3$, Journal of Applied Physics, 106(2009) 024102.

[24] R. Ranjan, R. Kumar, N. Kumar, B. Behera, R.N.P. Choudhary, Impedance and electric modulus analysis of Sm modified Pb $(Zr_{0.55}Ti_{0.45})1–x/4O_3$ ceramics, Journal of Alloys and Compounds, 509 (2011) 6388–6394.

[25] F. Li, J. Zhai, B. Shen, X. Liu, H. Zeng, Simultaneously high energy storage density and responsivity in quasi-hysteresis free Mn-doped $Bi_{0.5}Na_{0.5}TiO_3$-$BaTiO_3$-$(Sr_{0.7}Bi0.2–0.1)$ TiO_3 ergodic relax or ceramics, Materials Research Letters, 6 (2018) 345–352.

[26] X. Guo, W. Sigle, J. Fleig, J. Maier, Role of space charge in the grain boundary blocking effect in doped zirconiaolid State Ionics, 154–155 (2002) 555–561.

[27] B. Alzahrani, S. Hcini, S. Mnefgui, A. Dhahri, M.l. Bouazizi, Sintering temperature effects on the impendence spectroscopy properties of $Nd_{0.67}Pb_{0.33}Mn_{0.9}Al_{0.1}O_3$ perovskites, Phase Transitions, 93 (2020) 417–428.